Elaboration of the magnetically frustrated GeFe2O4 spinel thin films by pulsed laser deposition

Laurent Schlur, Corinne Bouillet, François Roulland, Gilles Versini, Marc Lenertz, Cédric Leuvrey, Jérôme Robert, Gilbert Chahine, Nils Blanc, Antonio Peña Corredor, et al.

Materials Chemistry and Physics 340 (2025) 130831

Contents lists available at ScienceDirect

Materials Chemistry and Physics

journal homepage: www.elsevier.com/locate/matchemphys

Elaboration of the magnetically frustrated $GeFe_2O_4$ spinel thin films by pulsed laser deposition

L. Schlur [a,*], C. Bouillet [b], F. Roulland [a], G. Versini [a], M. Lenertz [a], C. Leuvrey [a], J. Robert [a], G.A. Chahine [c], N. Blanc [d], A. Peña Corredor [a], D. Preziosi [a], C. Lefèvre [a], N. Viart [a]

[a] Université de Strasbourg, CNRS, IPCMS, UMR 7504, 23 rue du Loess, 67034, Strasbourg, France
[b] Université d'Orléans, CNRS, MACLE, UAR 2590, 1b rue de la Férollerie, 45071, Orléans, France
[c] SIMaP, Université Grenoble Alpes, CNRS, Grenoble INP, 38000, Grenoble, France
[d] Université Grenoble Alpes, CNRS, Grenoble INP, Institut Néel, 38000, Grenoble, France

HIGHLIGHTS

- Optimization of the PLD procedure used to obtain stoichiometric $GeFe_2O_4$ films.
- First obtention of low roughness, well-crystallised, epitaxial $GeFe_2O_4$ thin films.
- Possibility to tune the magnetic order temperature by changing the Fe/Ge ratio.

ABSTRACT

Magnetic frustration is a key research focus in condensed matter physics, where competing spin-spin interactions give rise to emergent phenomena that challenge conventional understanding and lead to topological effects with potential applications in quantum technologies. The direct spinel $GeFe_2O_4$ has recently garnered renewed interest for the plethora of magnetic behaviours it is able to demonstrate. Here, we report on the pioneering stabilization of $GeFe_2O_4$ thin films via pulsed laser deposition on MgO (001) substrates. The ablation procedure has been optimized to counterbalance the large volatility of the Ge species compared to the Fe ones, granting a fine control over the compositional homogeneity and stoichiometry of the films. Atomic force microscopy measurements rendered thin film surfaces with very low roughness values in the range of 0.2 nm, and X-ray diffraction data confirmed the epitaxial growth of the films and their high crystallinity with no detectable presence of spurious phases. SQUID magnetometry measurements revealed the expected antiferromagnetic behaviour, albeit with ordering temperatures higher than the expected bulk value. This discrepancy could be explained accounting for a small deviation from the direct spinel structure, as unveiled by resonant elastic X-ray scattering measurements, and from the resulting partial occupation of the tetrahedral sites by Fe atoms. Finally, varying the laser fluence we could tune the Fe/Ge ratio and provide a control over the ordering temperature from a modification of the spin-spin super-exchange network paths. Our results pave the way to further studies to explore emergent magnetic properties in $GeFe_2O_4$-based heterostructures.

1. Introduction

Research on frustrated magnetic materials is a very active field, as demonstrated by the extensive body of publications [1–7]. Among the magnetically frustrated materials, complex oxides with the AB_2O_4 spinel structure are of special interest due to the high frustration associated to the triangle-based geometry of the pyrochlore sublattice formed by their B sites [6]. In GeB_2O_4 compounds the antiferromagnetic behaviour is a pure result of the aforementioned highly frustrated pyrochlore sublattice [8–10].

Among this family, $GeFe_2O_4$ (GeFO), a mineral of rare natural occurrence also known as brunogeierite is of particular interest. GeFO is a direct spinel oxide crystallizing in the $Fd\bar{3}m$ space group with a lattice parameter of 8.4127(7) Å. Magnetic Fe^{2+} ions sit in the octahedral B sites while the non-magnetic Ge^{4+} ions are positioned in the tetrahedral A sites with the oxygen in a peculiar (u,u,u) position close to the u = 0.25 ideal case [11,12]. This close-to-ideal oxygen location makes GeFO the most symmetric of the spinel compounds, extremely attractive for magnetic frustration phenomena where equidistance is a key parameter. Perfectly stoichiometric GeFO can be seen as the archetype of the magnetically frustrated compound where all neighbours of the magnetic cation are equivalent [13].

Early studies have shown that GeFO was antiferromagnetic below *ca.* 10 K [14]. More recent results have demonstrated that there were in fact

* Corresponding author.
E-mail addresses: laurent.schlur@ipcms.unistra.fr (L. Schlur), nathalie.viart@ipcms.unsitra.fr (N. Viart).

https://doi.org/10.1016/j.matchemphys.2025.130831
Received 4 February 2025; Received in revised form 20 March 2025; Accepted 31 March 2025
Available online 1 April 2025

two magnetic transitions, at ≈ 9 K and ≈7 K [11]. Barton et al. also observed two magnetic transitions in GeFO, close to 8 K and 6 K [15]. Contrary to what is observed for other germanate spinels ($GeCo_2O_4$, $GeNi_2O_4$ [15,16]), the $GeFe_2O_4$ structure shows no distortion in the crystal structure and remains in the cubic $Fd\bar{3}m$ space group below the Néel temperature. Perversi et al. reported the presence of incommensurate long-range spin amplitude waves in $GeFe_2O_4$ [11]. They showed that one-third of the Fe^{2+} spins remained dynamic below the magnetic ordering transitions due to a frustration wave order in GeFO. The conclusion of the calculations performed by J. Luo et al. were different [17] and showed that GeFO can be described by a glassy magnetic state. These discrepancies in the scientific community show how much the frustration in GeFO is complex and can conduct to various different magnetic behaviours. One must note that the spinel structure of GeFO also holds potential for non-magnetic applications, including their use as an anode in lithium or sodium ion batteries [18–20] or as an electrocatalyst for urea oxidation reaction [21].

Although stoichiometric GeFO could be rather easily synthesized in its bulk form, both in single crystals [22,23] and powders [11], the high volatility of germanium oxides [24] makes the elaboration of stoichiometric GeFO thin films a very difficult task. There are only a few papers reporting the elaboration of $Ge_xFe_{3-x}O_4$ thin films [25–28]. Abe et al. elaborated GeFO films on Corning glass substrates by radio frequency sputtering but the highest x value they could reach is 0.3 [26,27]. M Seiki et al. deposited $Ge_xFe_{3-x}O_4$ films by pulsed laser deposition either on $SrTiO_3$ (111) substrates under an oxygen pressure or on Al_2O_3 (0001) substrates under vacuum [25,28]. The highest x value they could reach was of 0.94, obtained with the second conditions. There is no work in the literature that mentions obtaining a x = 1 compound. Nevertheless, this remains essential for achieving the theoretical antiferromagnetic behaviour. None of the mentioned papers studied the homogeneity of the Fe/Ge atomic ratio throughout the layer thickness, although this parameter can easily be subject to variations during the deposition process, as we will see later in this article.

Here we report a thorough study undertaken to grow $Ge_xFe_{3-x}O_4$ (001) thin films (with x in the [0.91–1.2] range) onto MgO (001) substrates, by pulsed laser deposition (PLD). To achieve a thermodynamic stability of the $GeFe_2O_4$ phase in the laser-induced plume, thereby allowing a good degree of stoichiometry and homogeneity of the epitaxial GeFO films, we considered several aspects of our ablation process, such as the nominal stoichiometry of the target, the ablation history and the preferential ablation of germanium over iron. As a result, we could obtain perfectly stoichiometric GeFO thin films. We extended the study to the tuning of the antiferromagnetic behaviour of the GeFO thin films by varying the kinetics of the ablation process itself. In particular, the ordering temperatures could be varied through the control of the partial occupation of the tetrahedral sites by Fe ions. The cationic distribution of the GeFO spinel structure in the thin films was determined with precision by resonant elastic X-ray scattering (REXS) measurements.

2. Materials and methods

Thin films of GeFO were grown on MgO (001) substrates (Codex International) by PLD. Two mixed-phase ceramic targets of different molar compositions, [GeO_2:Fe_2O_3] = 1:1 or 1:1.5, were obtained by sintering a mixture of Fe_2O_3 (Strem Chemicals 99.8 %), and GeO_2 (Rhône-Poulenc 98 %). These precursors were weighed in appropriate proportions, then manually milled and ground for 20 min in an agate mortar using ethanol as a dispersive solvent. The slurry was then dried into an oven. The resulting dry powder was finally uniaxially pressed, using a 1.5 T cm^2 load, into a 26 mm diameter pellet which was then sintered at 1100 °C for 10 h in air.

After optimization, the PLD deposition temperature is fixed to 400 °C. This temperature is low enough to reduce unwanted diffusion phenomena between the substrate and the film at the interface while still permitting a high degree of crystallisation for the film. An argon deposition atmosphere (0.05 mbar) has been used so that Fe can be kept in its +2 valence state. A KrF excimer laser (Coherent-Compex Pro 102F, λ = 248 nm) is used to hit the target at an angle of 45° and with an imprint of 1.05 mm^2. The laser fluence was varied between 2.5 and 3.3 J cm^{-2}, and adjusted to reach the desired Fe/Ge atomic ratios. One frequency of the laser was used: 5 Hz. The substrate is placed in front of the target at a distance of 50 mm. Various procedures have been used to scan the target with the ablating laser, among which continuous scanning with overlapping laser spots with or without an important preablation or, on the opposite, isolated discrete spots. Each procedure is explained into details in the following parts.

The growth mode and crystallinity of the layers were characterized in situ at the end of the deposition by reflection high energy electron diffraction (RHEED). The composition of the samples, both target and films, was determined by energy dispersive X-ray spectroscopy (EDX) coupled to a JEOL 6700F scanning electron microscope (SEM). Atomic force microscopy (AFM) was performed with a Park XE7 (Park System) in true non-contact mode in order to quantitatively estimate the roughness of the films. The structure of the bulk target samples was determined by X-ray diffraction with a D8 Discover diffractometer equipped with a Cu Sealed tube (λKα1 = 0.15406 nm), a quartz front monochromator, a motorized anti-scatter screen and an energy resolved Lynxeye XE-T linear detector. θ-2θ scans were then performed in the Bragg Brentano geometry. The structural characterization of the thin films, with θ-2θ scans, ϕ scans, and reciprocal space mappings (RSM), was performed in parallel beam geometry with a Smartlab Rigaku thin film diffractometer equipped with a 9 kW copper rotating anode and a double bounce Ge(220)x2 front monochromator ($K_{\alpha 1}$ = 0.15406 nm). The same set-up was used to perform X-ray reflectivity (XRR) and check the thickness of the films. Transmission electron microscopy (TEM) was performed with a JEOL 2100F Cs corrected, operating at 200 kV, with a 0.2 nm point to point resolution in TEM and 0.1 nm in scanning TEM mode (STEM). The TEM set-up was also used to determine the elemental composition at a nanometric scale using a SDD EDX spectrometer. The germanium and iron contents were determined using the K-shells. The magnetic properties were determined using a superconducting quantum interference device magnetometer (SQUID VSM MPMS 3, Quantum Design). The temperature dependence of the samples magnetization was measured from 2 to 250 K under a field ranging between 0.005 and 0.1 T, in both zero-field-cooled (ZFC) and field-cooled (FC) modes. The magnetization (M) versus the magnetic field (H) were also measured with a field ranging between + and - 7 T and temperatures between 10 and 300 K. The measurements were performed in the parallel configuration, i.e. with the applied magnetic field parallel to the sample. The cationic distribution could be determined from Resonant Elastic X-ray Scattering (REXS) experiments in the X-ray Absorption Near Edge Structure (XANES) domain (also known as Diffraction Anomalous Near Edge Structure (DANES)). REXS spectra were acquired at the Ge edge (11.1 keV), spanning by 50 eV below and above the edges, for the 111, 115, 202, 333 and 422 reflections. The synchrotron experiments were carried out on the collaborating research group (CRG) D2AM beamline at the European Synchrotron Radiation Facility (ESRF, Grenoble) [29]. Samples were mounted on a seven-circle diffractometer equipped with various photodiode detectors allowing recording the intensity of the incident beam I_0, the intensities of the diffraction peaks and the fluorescence of the samples. The rotation matrix was preliminary determined with the help of different in-plane and out-of-plane reflections. Anomalous factors f' and f'' were extracted from the fluorescence data. The knowledge of f_0, f' and f'' allows the simulation of the scans for a given set of structural parameters. The refinement of the experimental spectra was performed by minimizing the sum of all reliability factors for all reflections and edges through a stochastic basin-hopping algorithm (FitREXS program [30]).

3. Results and discussion

3.1. Standard ablation conditions

First thin films depositions were performed by directly ablating the as-prepared mixed-phase target [GeO_2:Fe_2O_3] = 1:1.5, without any pre-ablation process. The laser fluence and repetition rate were 2.5 J cm^{-2} and 5 Hz, respectively. Fig. 1 schematizes the laser displacement on the target surface during a standard ablation procedure, with, for clarity's sake, deliberately increased sizes and decreased numbers of laser impacts with respect to reality. The imprint of the laser can be approximated to a rectangle (in reality the corners are rounded) having a height of 1.5 mm and a width of 0.8 mm. The ablated pattern consists of 50 lines of 100 spots each. The horizontal distance between two consecutive spots is 0.06 mm and the vertical distance between two consecutive lines is 0.09 mm. A deposition is made by repeating the pattern 4 times, resulting thus in 20 000 counts.

Films deposited with this procedure were characterized by STEM and STEM-EDX in cross section (Fig. 2). The films are 16 ± 1 nm thick (Fig. 2a), which corresponds to a 0.24 nm min^{-1} growth rate. The composition profile of the cross section determined by EDX elemental analysis is presented on Fig. 3b and c. The atomic concentration of iron (germanium) increases (decreases) with the thickness of the film, resulting in an increase of the Fe/Ge atomic ratio. The value of this atomic ratio spans from 1.1 at the substrate-film interface to 2.5 at the surface of the film. Considering the nominal stoichiometry of the [GeO_2:Fe_2O_3] = [1 : 1.5] target, one should observe a Fe/Ge atomic ratio of 3. The experimental value is thus lower than the expected one within the whole film thickness. Moreover, when closely looking at Fig. 2c one can note that the Fe/Ge atomic ratio is not linearly increasing as a function of the distance from the substrate, but rather increases by steps of ca. 1–2 nm followed by a stable period of 2–3 nm.

PLD has earned its spurs as excellent method for depositing complex oxides as it allows stoichiometric transfer from the target to the film. One of its major achievements is probably the first successful preparation of thin films of Y–Ba–Cu–O superconductors [31]. This stoichiometric transfer relies on the fast and strong heating of the target surface by the intense laser beam which results in a global transfer of the target material as a high temperature plasma [32]. However, there are also some reports of non-stoichiometric transfer in PLD processes [33]. Among the mechanisms proposed for the deviation from stoichiometry, one can cite preferential ablation of one compound from the target, preferential re-sputtering by the ablated species at the films surface or differential scattering of the ablated species in the chamber atmosphere. In the case of PLD elaboration of GeFO, stoichiometry is a major issue, as reported by Seki et al. [28] who could only reach a $Ge_{0.94}Fe_{2.06}O_4$ composition, using a target with a GeO_2:Fe_2O_3 molar ratio of 12:1. The stoichiometric transfer is probably majorly jeopardized by the fact that Ge species have a greater tendency to volatilization than Fe ones [24,34,35].

The evolution observed in Fig. 2 can also be explained by the preferential ablation of the germanium species with respect to the iron ones, which induces a modification of the target surface composition after each laser impact. The higher the number of impacts, the higher the concentration of the target in Fe species. This evolution of the Fe–Ge composition of the target during ablation can be easily understood by referring to the sketches shown in Fig. 1. The darker regions correspond

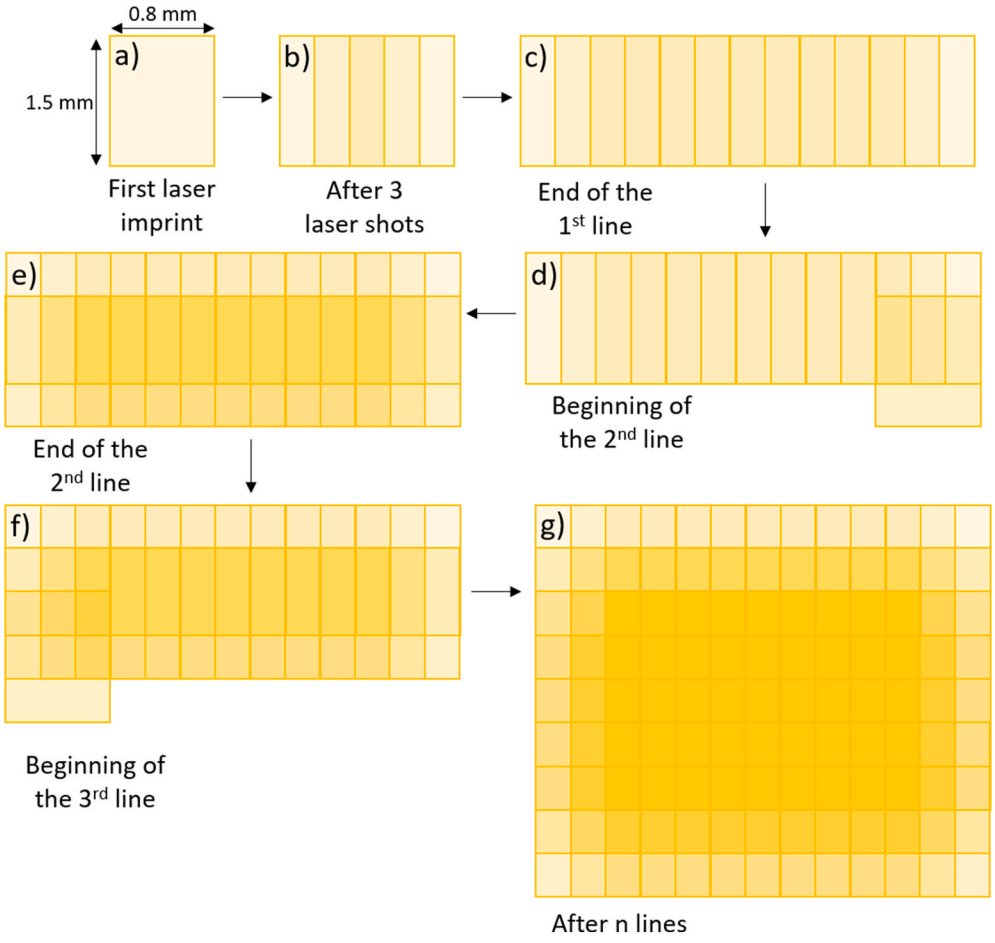

Fig. 1. Scheme of the laser shots path on the target surface during a classical ablation procedure. a) first laser imprint, b) after three laser shots, c) end of the first line, d) beginning of the second line, e) end of the second line, f) beginning of the third line and g) after n lines. For clarity's sake, the ratio between the laser spot width (height) and horizontal (vertical) displacement is 3 (3) here, instead of 14 (17) for the real sizes.

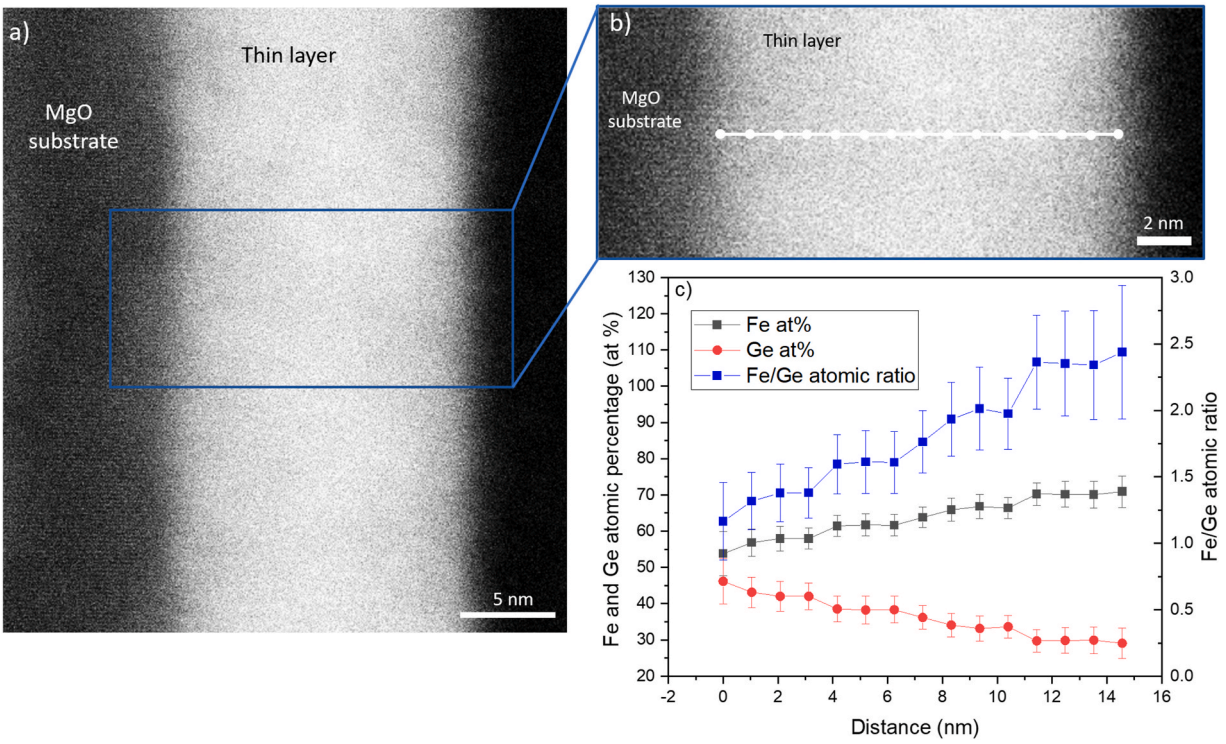

Fig. 2. a) and b) STEM cross section images of the film deposited in classical ablation conditions. c) STEM-EDX elemental analysis showing the evolution of its iron and germanium composition and of its Fe/Ge atomic ratio in the cross section. The experimental points presented on Figure c) correspond to measurements performed on the spots indicated on Figure b).

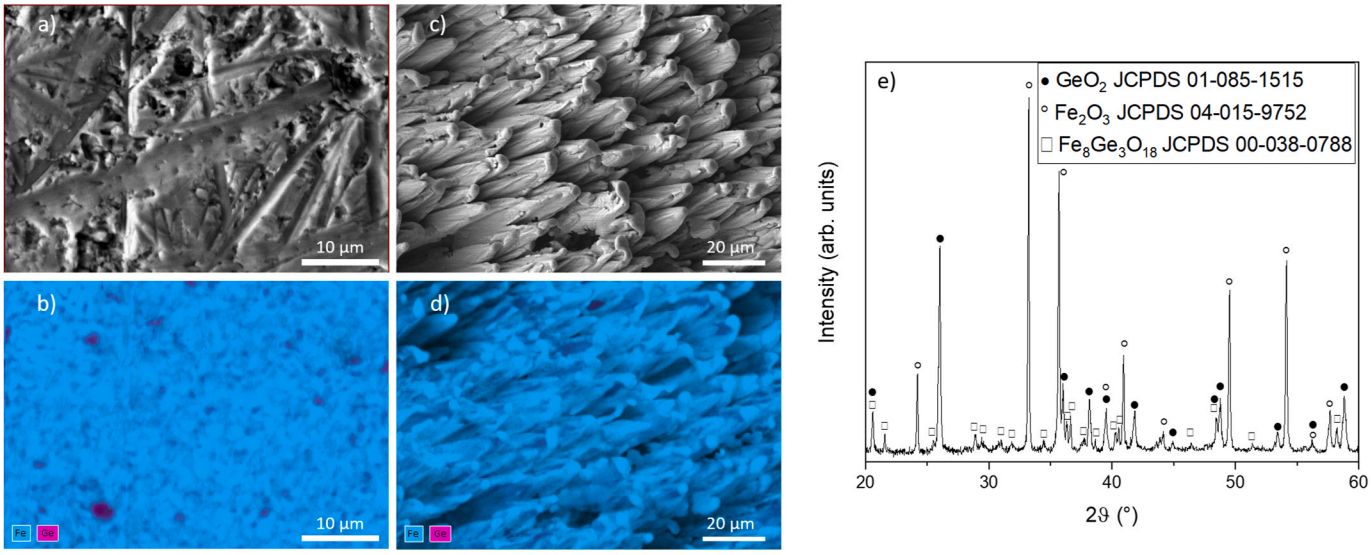

Fig. 3. a), c) SEM images b),d) SEM EDS Maps (net sum) of the [GeO_2: Fe_2O_3] = [1 : 1.5] target surface, a) and b) correspond to the same surface of the target before ablation, c) and d) are obtained after the standard ablation procedure, e) X-ray diffractogram of the unablated [GeO_2: Fe_2O_3] = [1 : 1.5] target.

to the areas with higher number of laser shots so with the lowest (highest) concentration in germanium (iron).

When considering the ratio between the height of the laser impact (1.5 mm) and the vertical displacement of the impacts (0.09 mm), one can see that it is only after 17 lines (3 in the illustrative Fig. 1) that the laser will hit similarly impacted areas. So, due to the preferential ablation of Ge, a stable composition in Fe and Ge can only be reached after 17 lines for each pattern (17 x 100 spots, i.e. 1.4 nm), if neglecting the first 14 shots of each line (which correspond the 0.8 mm width of the laser spot divided by its 0.06 mm horizontal displacement) for which the Fe/Ge composition is not yet stable (this only represents a thickness of 0.01 nm). The rest of the pattern, (50 minus 17) lines x 100 spots, corresponds to a deposition thickness of 2.6 nm. This explains why one observes a 1–2 nm of increase in the Fe/Ge ratio followed by a stable period of 2–3 nm four times, since the pattern is repeated four times.

To confirm that the germanium species of the target are preferentially ablated with respect to the iron species, the target has been studied by SEM EDS and X-ray diffraction before and after ablation (Fig. 3).

The target before the ablation process, as imaged by SEM (Fig. 3a), is smooth and dense; these are perfect properties for suitable ablation

processes. Its analysis with EDS gives an overall Fe/Ge atomic ratio of 2.9 ± 0.3, in perfect agreement with the expected composition for [GeO_2: Fe_2O_3] = 1:1.5. Fig. 3b shows Fe- and Ge-rich regions, randomly dispersed. The area of these regions (*ca.* 1 μm^2) is significantly smaller than that of the laser beam (1 mm^2), which ensures that the ablated zone is homogeneous with respect to the size of the beam and has the global expected composition. The X-ray diffraction (Fig. 3e) reveals that the target is composed of a significant amount of GeO_2 and Fe_2O_3 and a smaller quantity of $Fe_8Ge_3O_{18}$.

After the ablation process, the aspect of the target is totally different (Fig. 3c) from what it was before ablation. Its surface takes a columnar-like shape mainly composed of iron species. The composition of the apex of each column is very close to being 100 % iron species. The Fe/Ge atomic ratio of the entire Fig. 3d (ablated target) is 6.0 ± 0.3, which is the double of the initial value (Fig. S1). This result confirms that during the ablation germanium is preferentially ablated with respect to iron, which remains on the target as the main component. Similar observations can be made on the [GeO_2: Fe_2O_3] = 1:1 target (Fig. S2).

In order to overcome the problem of germanium preferential ablation and in order to obtain films with a homogeneous composition, two other ablation procedures have been tried. With a first procedure consisting in a long pre-ablation of the mixed-phase target, the composition of the film was still inhomogeneous. This procedure and the results associated with it are described in the supporting information. The second procedure is described below.

3.2. Ablation from target spots of identical history

The previous paragraphs show that the composition of the target is modified after each laser impact, which results in a modified composition of the deposited film. We have therefore looked for a way to ablate spots of perfectly identical ablation-history. Fig. 4 presents a scheme of the developed strategy.

In this procedure, the ablation is performed in lines, with a horizontal shift between two consecutive laser impacts of 0.004 mm. A pre-ablation is first performed on this line for 500 impacts, before ablation proceeds, still on the same line, keeping the 0.004 mm distance between two consecutive spots. The first 200 spots (the 0.8 mm laser width divided by its 0.004 mm horizontal displacement) of the pre-ablation will have non-identical ablation history, but they do not contribute to the elaboration of the film. The ablation includes 2500 shots. With only 2500 shots, the thickness of the layer would be quite thin. A second line, 9 mm distant from the first one, is thus also pre-ablated and then ablated. The distance is fixed to 9 mm in order to prevent any overlap

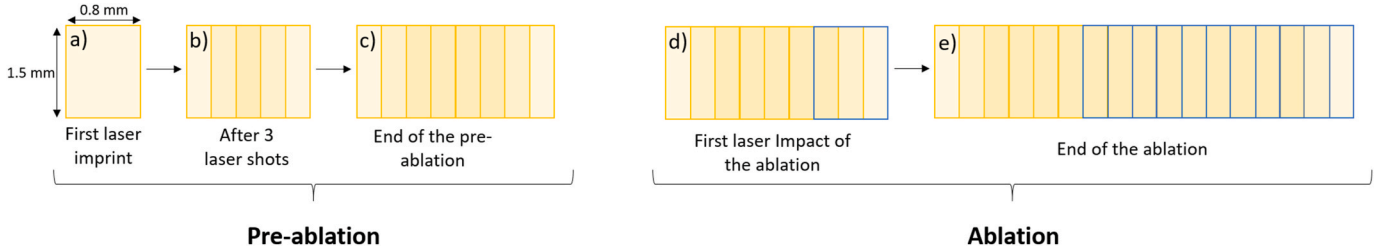

Fig. 4. Scheme of the target surface ablation with the optimized procedure. a) first laser imprint, b) after three laser shots, c) at the end of the pre-ablation, d) first laser impact of the ablation, e) end of the ablation.

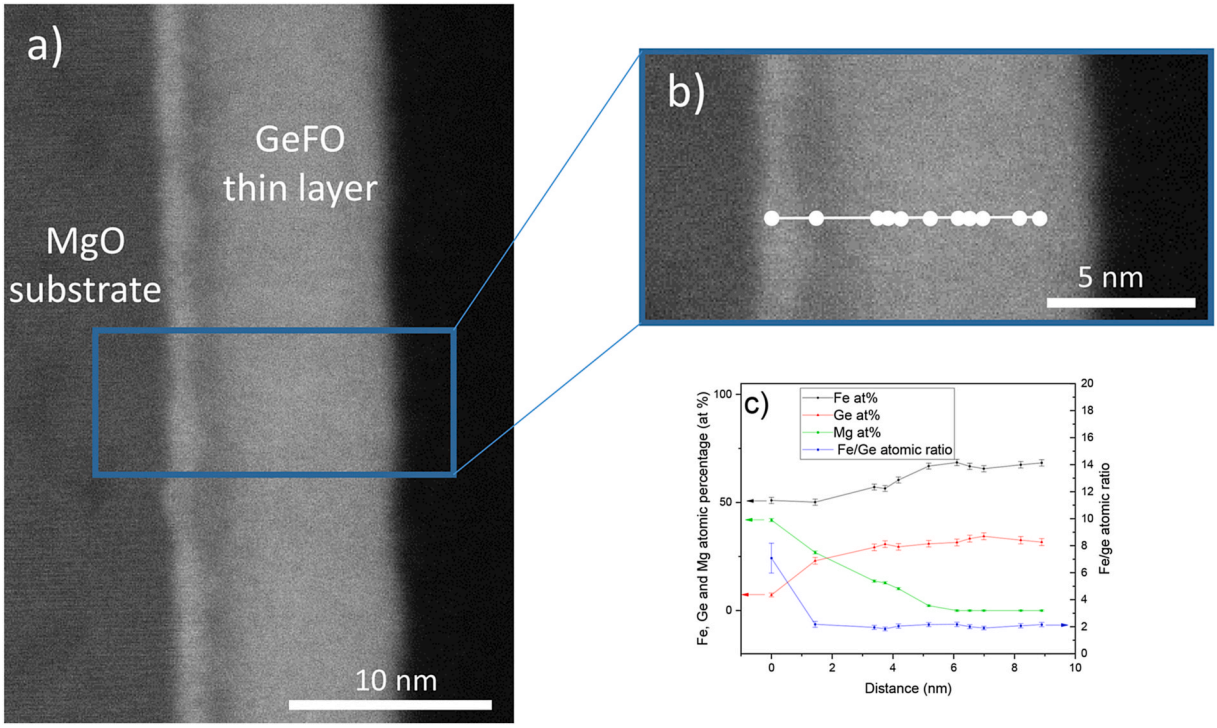

Fig. 5. a) and b) STEM cross section image of the film obtained with an identical spot state. c) Variation of its iron, germanium and magnesium composition and of its Fe/Ge atomic ratio in the cross section determined by STEM-EDX.

between the two lines, as well as to reduce the amount of matter redeposition coming from the other line. The two lines were first pre-ablated and then ablated with no interruption during the ablation.

The repetition rate of the laser is fixed to 5 Hz, the fluence to 3.1 J cm^{-2} and the $[GeO_2:Fe_2O_3]$ = 1:1.5 target has been ablated. The composition of the films thus deposited has been analysed in cross section by STEM and EDX (Fig. 5).

Apart from a very thin (≈1 nm) interfacial layer which is Mg and Fe rich, the film is homogeneous in composition, with an Fe/Ge atomic ratio of about 2 all along its thickness. The mean ratio value, without considering the interdiffusion zone, is equal to 2.0 ± 0.1 which is in total agreement with the expected value. This ablation procedure thus allows the growth of homogeneous $GeFe_2O_4$ films. The darker line seen on the film (Fig. 5a and b) is due to the diffusion of magnesium from the substrate into the GeFO layer (Fig. 5c), showing that despite the low deposition temperature there are still some diffusion phenomena. The total thickness of the film, determined by STEM, is equal to 11 ± 1 nm.

The RHEED pattern of the GeFO film at the end of the deposition shows a rather streaky pattern (Fig. 6a), as expected for a layer-by-layer growth, with the presence of Kikuchi lines indicating both low roughness and high crystallinity of the thin film. This is confirmed by AFM measurements rendering the very low RMS roughness of circa 0.19 ± 0.05 nm (Fig. 6b). The films are well crystallised, perfectly (00*l*) oriented and exempt from any spurious phase, as can be seen in the θ-2θ X-ray diffraction patterns (Fig. 6b). Due to the proximity of the GeFO out-of-plane inter-reticular distances with those of MgO, the GeFO XRD peaks are hidden by those originating from the MgO substrate. However, the presence of the GeFO film, as well as the quality of its interfaces, is well indicated by the Laue fringes around the MgO (00*l*) peaks. ϕ-scans performed around the 026 and 024 reflections of GeFO and MgO, respectively, indicate a cube-on-cube growth (Fig. 6d). This result is confirmed with the 115 reflection of GeFO. The RSM of the GeFO (115) node (Fig. 6e) is compatible with a GeFO film fully matching in-plane with the MgO substrate parameter (a = 4.21 Å), i.e. fully stressed by the substrate. One should notice that this does not imply any important strain for GeFO since the mismatch between GeFO and MgO is only of 0.08 %. The out-of-plane GeFO cell parameter deduced from the RSM is 8.412 ± 0.002 Å, also very close to the GeFO bulk parameter of 8.413 ± 0.001 Å. The thickness determined by XRR, 11.67 ± 0.02 nm, is in agreement with the value determined by STEM (11 ± 1 nm). The SEM-EDS analysis gives a Fe/Ge atomic ratio of 2.0 ± 0.1 which confirms the value obtained by STEM-EDX.

A magnetic characterization of the film was performed by FC/ZFC measurements under various magnetic fields between 50 and 1000 Oe (Fig. 7). The MgO substrates contain impurities whose paramagnetic behaviour is predominant to their expected diamagnetic one at low temperatures, as visible on Figure S3 a) and b). On Fig. 7, the paramagnetism of the MgO substrate was subtracted, but the curves were not corrected from the diamagnetism of the substrate, which explains why the plotted value of susceptibility is negative. All plots show a maximum at about 40 K, indicating a transition towards an antiferromagnetic state. This transition is not due to the MgO substrate as it is not visible on the ZFC curve of the substrate alone (Fig. S3a). This susceptibility maximum of *ca.* 40 K is higher than those reported in the literature (≈10 K) for

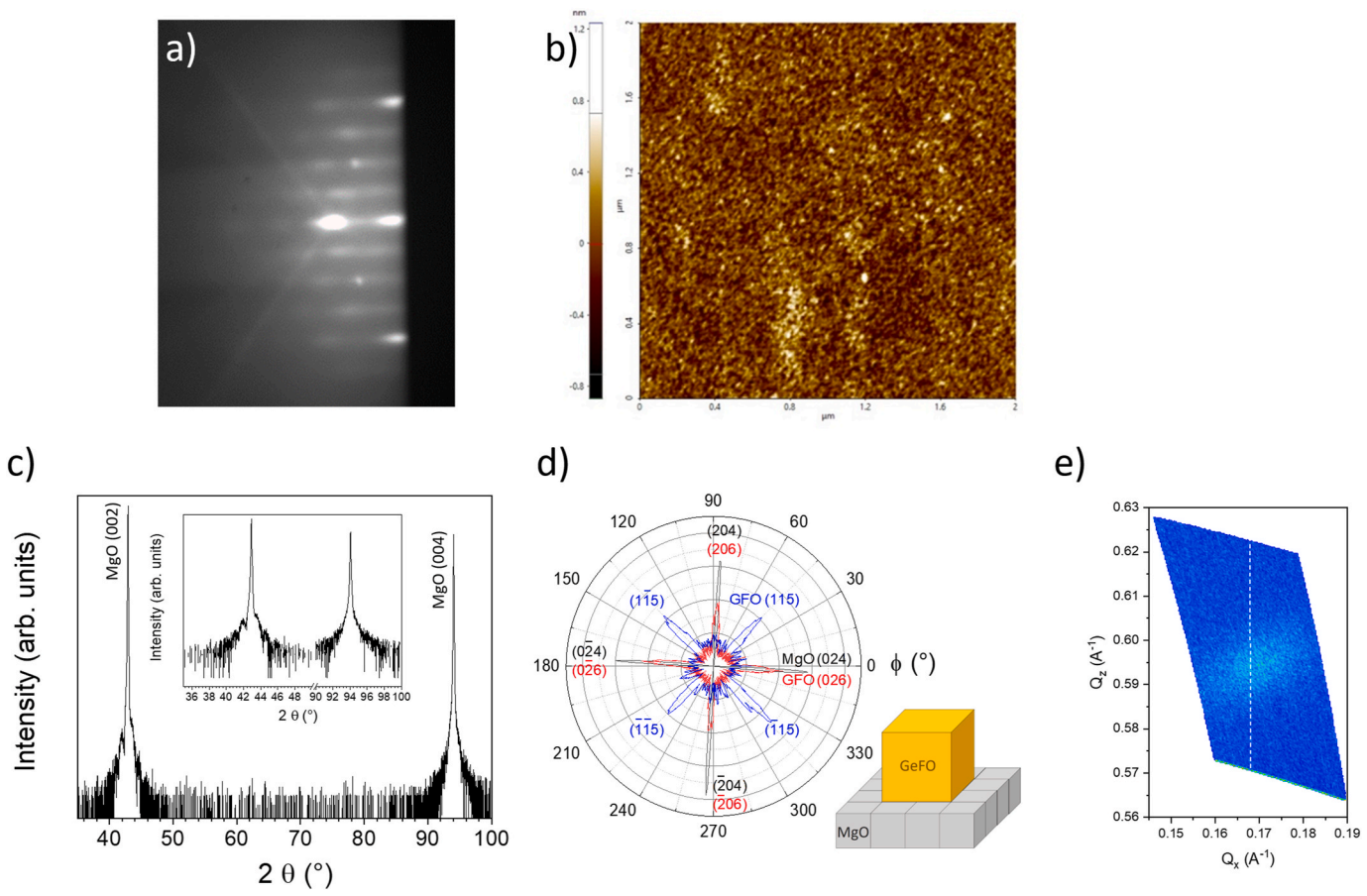

Fig. 6. Morphological and structural characterization of the film grown in the optimized conditions. a) RHEED along the [110] direction of the substrate, b) AFM topography (2 × 2μm^2), c) θ-2θ X-ray diffraction patterns, (d) φ-scans around the GeFO 026 and 115 and MgO 024 reflections together with the scheme of the GeFO on MgO cube on cube growth they allow to conclude to and (e) RSM of a GeFO 115 reflection. The dashed white line indicates the expected Q_x position for a GeFO film fully matching in-plane with the MgO substrate.

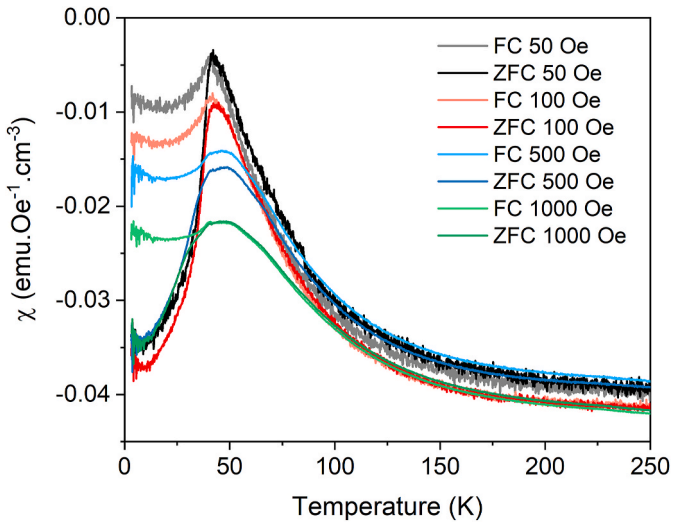

Fig. 7. FC and ZFC measurements of optimized GeFO samples under various fields between 50 and 1000 Oe. The clear maximum at about 40 K, indicates a transition towards a strong antiferromagnetic state.

GeFO, but one has to note that these reported values are for polycrystalline samples [11,15].

This discrepancy could be due, at least partially, to a different cationic distribution within the sample. A very small deviation from the expected total occupation of the octahedral sites by Fe and of the tetrahedral sites by Ge will yield extra magnetic exchange paths, and in particular additional A-O-B super-exchange paths. Those A-O-B exchanges are known to be the strongest in spinels due to significant orbital overlaps facilitated by the nearly 180° A-O-B bond angles [36]. Magnetization versus magnetic field curves were also measured at different temperatures between 10 and 300 K for both an MgO substrate alone and a sample featuring a GeFO film (Figs. S3b and c). The presence of paramagnetism for the MgO substrate alone is clearly visible at 10 K (at higher temperatures the negative slope of the curve is due to diamagnetism, as expected) and the curves measured for both samples are in fact very similar. The sample with the GeFO film seems to show more diamagnetism than the MgO substrate alone, but the slope variations between the two samples could well be explained by the variable amount of paramagnetic impurities from one MgO substrate to another one. The only significant difference between the two samples is the presence of an opening in the hysteresis loop clearly visible at 10 K when the sample features a GeFO film. This is compatible with a ferrimagnetic behaviour resulting from the presence of some Fe atoms in the tetrahedral sites of GeFO.

We have used a resonant X-ray diffraction technique to determine the cationic distribution in our GeFO thin films, following a method already optimized by some of the authors for other oxides [30]. Once the anomalous factors extracted from fluorescence, the refinement of all the recorded spectra was carried out using the FitREXS code, which uses a Basin-hopping optimization approach [37]. This method iterates by performing random perturbation of free parameters, performing local optimization, and accepting or rejecting new parameters based on a minimized function value and a probability cost.

Measurements were conducted at the Ge edge for selected hkl Bragg reflections. Fig. 8 presents the computed results for both direct and inverse spinel configurations at specific reflections, obtained using the FDMNES software [38]. A pronounced difference is observed, highlighting the capability of probing the cationic distribution solely via the Ge edge.

Fig. 9 shows the spectra recorded for the film at the germanium edge together with the results of the refinements. The refined free parameter is the cationic distribution y, of the theoretical formula: $(Ge_{1-y}Fe_y)_{Td}[Ge_yFe_{2-y}]_{Oh}O_4$.

The results of the refinement lead to a cationic distribution of $(Ge_{0.81}Fe_{0.19})_{Td}[Ge_{0.19}Fe_{1.81}]_{Oh}O_4$. This indicates that a small amount of iron is in the tetrahedral sites, and might explain that the magnetic transition observed in Fig. 7 occurs at a higher temperature than the value reported in the literature.

One must note that the physical properties of the GeFO films can easily be tuned using the Fe/Ge ratio as a lever. Using the optimized ablation procedure described before, with a laser repetition rate of 5 Hz and a $[GeO_2{:}Fe_2O_3]$ = 1:1.5 target composition, and only varying the

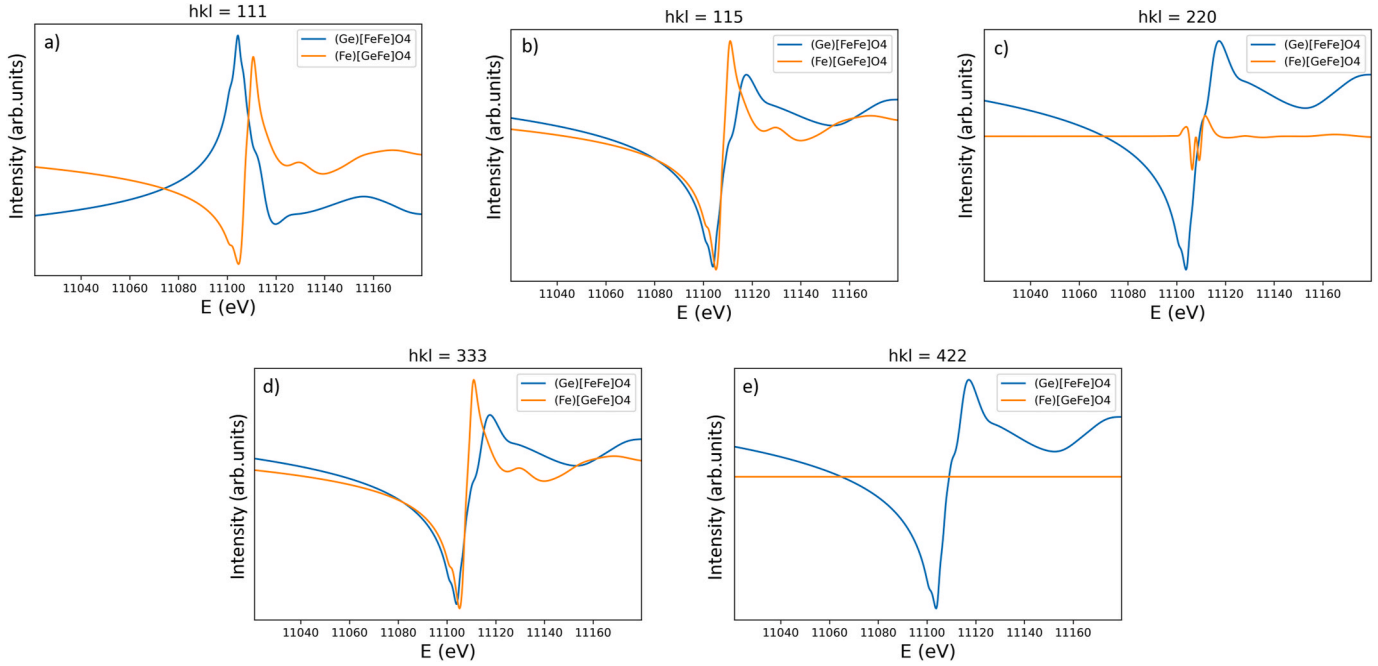

Fig. 8. REXS theoretical spectra computed for both direct and inverse $GeFe_2O_4$ spinel configurations at the Ge a) 111, b) 115, c) 202, d) 333 and e) 442 reflections with FDMNES software [38].

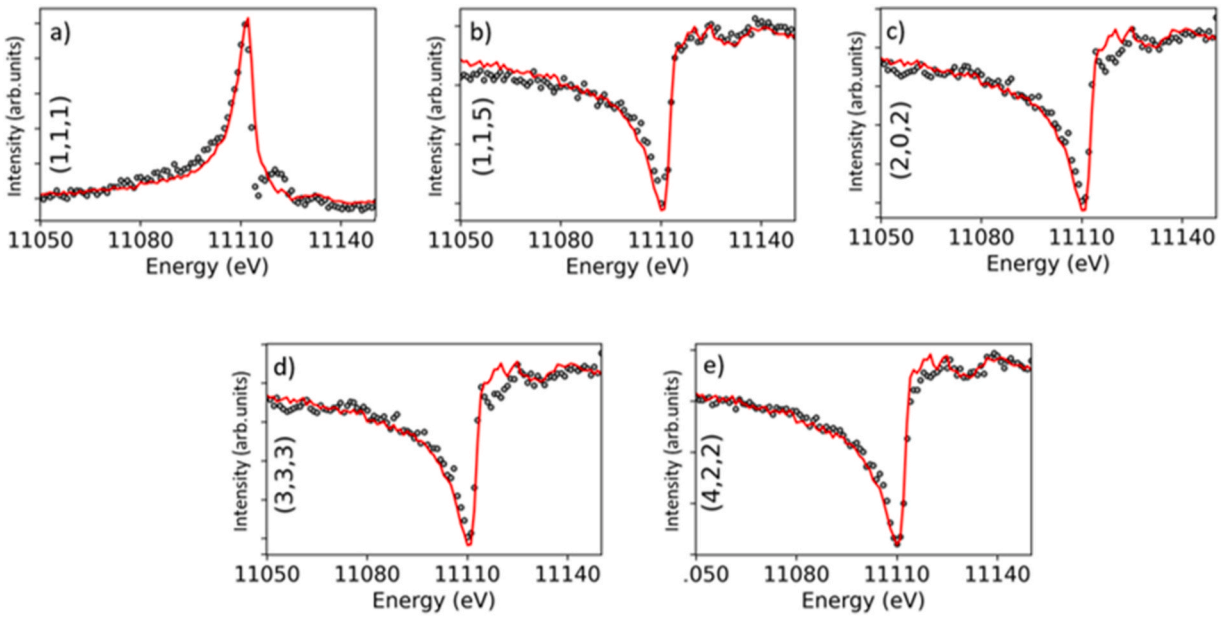

Fig. 9. REXS experimental spectra for the Ge a) 111, b) 115, c) 202, d) 333 and e) 442 reflections (grey points) and fit with the spectrum simulated for the best y free parameter value (y = 0.19) (red curves). (For interpretation of the references to colour in this figure legend, the reader is referred to the Web version of this article.)

laser fluence between 2.6 and 3.3 J cm^{-2}, we were able to obtain $Ge_xFe_{3-x}O_4$ thin films of homogeneous composition with various Fe/Ge ratios. Fig. 10 presents the evolution of the Fe/Ge atomic ratio (determined by SEM-EDS) of the film with the laser fluence.

The Fe/Ge ratio decreases with increasing laser fluences. Higher laser energies seem to promote the ablation of the germanium species in the target. With this method, and with the tested fluence range, it was possible to vary the Fe/Ge ratio from 1.5 ± 0.2 to 2.3 ± 0.1, which corresponds to films with compositions between $Ge_{1.20}Fe_{1.80}O_4$ and $Ge_{0.91}Fe_{2.09}O_4$.

For Fe/Ge ratios between 1.8 and 2.3 (corresponding to laser fluences between 3.25 and 2.6 J cm^{-2}), the RHEED patterns at the end of the depositions still show a streaky pattern (Fig. S4). The low roughness of the films is confirmed by AFM, with RMS roughness values lower than 0.2 nm (Fig. S5). By further increasing the laser fluence to 3.3 J cm^{-2} we obtained GeFO films with a Fe/Ge atomic ratio of 1.5 which were amorphous.

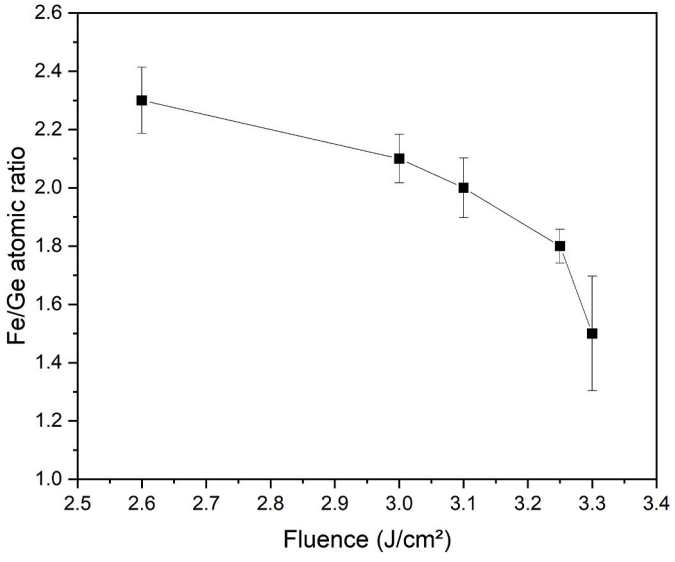

Fig. 10. Evolution of the Fe/Ge atomic ratio with laser fluence. The ratio has been determined by SEM-EDS.

In the remainder of this article, the samples thus obtained with different laser fluences will be referred to through their Fe/Ge atomic ratio and not through the fluence used, but it should not be forgotten that these samples with different Fe/Ge ratios were obtained by varying the laser fluence.

The structure of the films was characterized by X-ray diffraction (Fig. 11). For Fe/Ge ratios between 1.8 and 2.3, the films are well crystallised, perfectly (00*l*) oriented and exempt from any spurious phase, as can be seen on the θ-2θ X-ray diffraction patterns (Fig. 11a–c). The peaks originating from GeFO are not visible for a ratio of 2.1 (Fig. 11b) because they are hidden by those due to the MgO substrate, as expected since GeFO bulk parameters are very similar to those of MgO (4.21 Å). For a ratio of 1.8 the GeFO (00*l*) peaks start to be visible on the left of the MgO ones (Fig. 11a), which means that the out of plane parameter is higher than that of bulk GeFO. For a ratio of 2.3, the GeFO peaks are visible on the right of the MgO ones (Fig. 11c), indicating a lower out of plane parameter. These results are confirmed by RSM measurements of the GeFO 115 reflection which allow the determination of both in-plane and out-of-plane parameters (Table 1). The films are all fully strained by the substrate with an in-plane cell parameter of 8.42 (=2x4.21 = 2 x a_{MgO}) Å. The variation of the out-of-plane cell parameters with the Fe/Ge ratio is plotted in Fig. 11d. Its increase with the decrease of the Fe/Ge ratio can be explained by the evolution of the amount of iron and germanium in the layer, and by the modification of the cations ionic radius which varies with their crystallographic position (tetrahedral or octahedral) and with their oxidation state.

The homogeneity of the ratio throughout the film thickness has been analysed in cross section by STEM and STEM-EDX for the films with the highest and lowest Fe/Ge atomic ratios, i.e. 1.8 and 2.3, respectively (Figure S6 and Figure S7). Apart from a small region at the interface with the substrate, which is slightly deficient in germanium (similarly to what was observed for the x = 2.0 sample in Fig. 5), the films are homogeneous in composition all along their thickness, confirming that the optimized ablation procedure allows the growth of homogeneous $Ge_xFe_{3-x}O_4$ films. The mean ratio values determined by STEM-EDX, without considering the interdiffusion zone, are equal to 1.8 ± 0.1 and 2.4 ± 0.1, and perfectly match with the values determined by SEM-EDX of 1.8 ± 0.1 and 2.3 ± 0.1.

The Fe/Ge atomic ratio also influences the magnetic properties of the

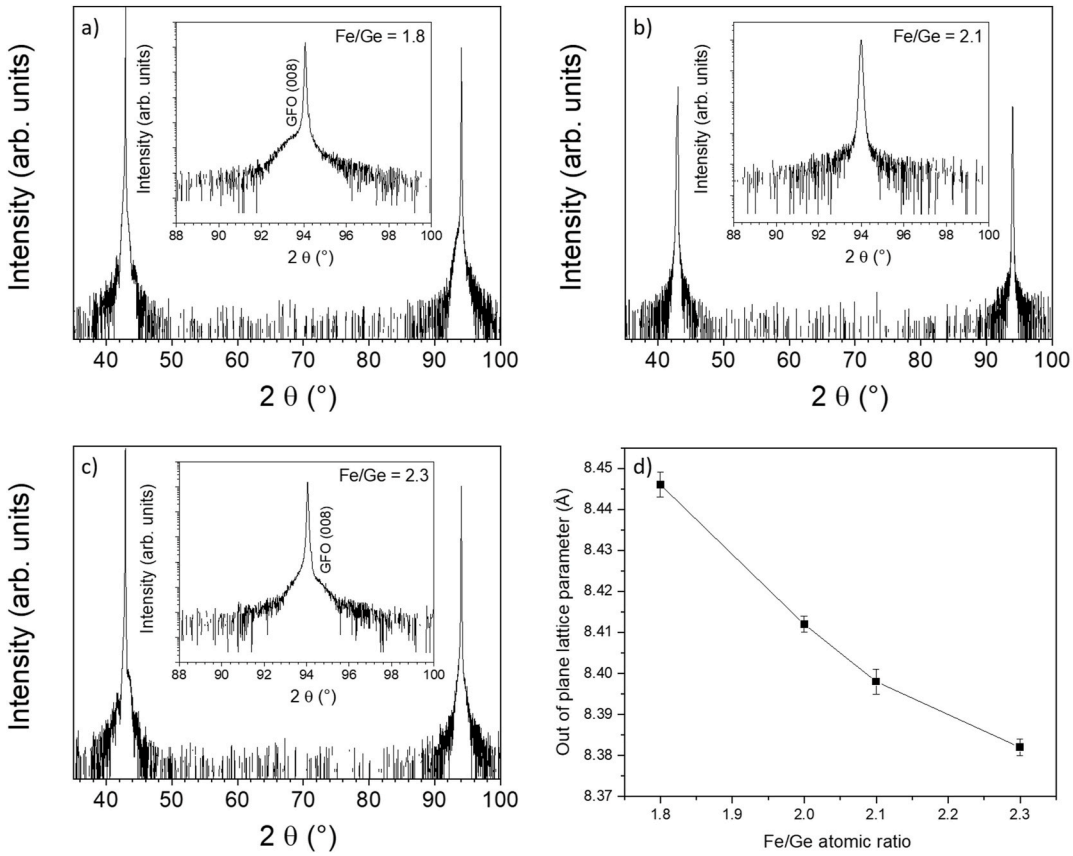

Fig. 11. Structural characterization of films with different Fe/Ge atomic ratios. θ-2θ X-ray diffraction patterns of the layers with a ratio of a) 1.8 ± 0.1, b) 2.1 ± 0.1and c) 2.3 ± 0.1. d) Evolution of the out of plane lattice parameter with the Fe/Ge composition. The out of plane lattice parameters were determined from the RSM of a GeFO 115 reflection.

Table 1
Evolution of the in-plane and out-of-plane lattice parameter with the Fe/Ge atomic ratio.

Fe/Ge	1.5 ± 0.2	1.8 ± 0.1	2.0 ± 0.1	2.1 ± 0.1	2.3 ± 0.1
In-plane parameter - a (Å)	amorphous	8.42 ± 0.01	8.42 ± 0.01	8.42 ± 0.01	8.42 ± 0.01
Out-of-plane parameter - c (Å)	amorphous	8.446 ± 0.003	8.412 ± 0.002	8.398 ± 0.003	8.382 ± 0.002

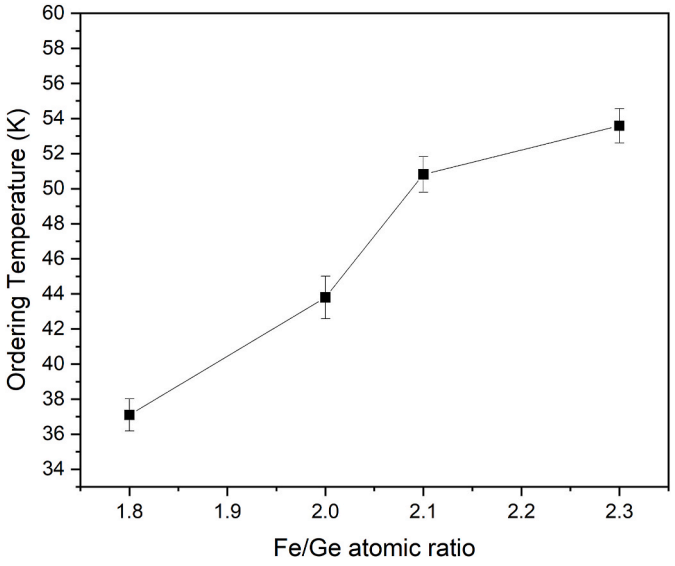

Fig. 12. Evolution of the ordering temperature of the films with their Fe/Ge atomic ratio. The temperatures were obtained from ZFC measurements.

films. The magnetic properties of each film were studied through Zero Field Cooled measurements under 100 Oe. The ordering temperature determined by these measurements was plotted as a function of the Fe/Ge ratio on Fig. 12.

The lowest value of 37 ± 1 K is obtained for the lowest Fe/Ge ratio of 1.8. It is still higher than the value of ca. 10 K observed for polycrystalline stoichiometric GeFO samples [11,15]. This is due to the fact that even for this low Fe/Ge ratio, there are still some Fe ions in the tetrahedral sites, yielding some A-O-B super-exchange pathways, and increasing the ordering temperature. The cationic distribution has been checked by REXS (Fig. S8) and indeed shows some Fe in the tetrahedral sites with a formula of $(Ge_{0.98}Fe_{0.02})[Ge_{0.09}Fe_{1.91}]O_4$.

4. Conclusions

We report here the first elaboration of stoichiometric $GeFe_2O_4$ thin films by pulsed laser deposition. The high volatility of the Ge species makes it very difficult to control the stoichiometry of the films. Various strategies have been tested and we understood that the history of the ablated target area plays a crucial role in the composition and homogeneity of the deposited film. The same was put forward by some of the authors also in the case of nickelate thin films [39]. We found that only by keeping the same ablation history for each target area we could

obtain films with the expected Fe/Ge = 2 stoichiometric ratio over the entire thickness. The films have RMS roughness values lower than 0.2 nm and grow epitaxially cube-on-cube on the MgO (001) substrate with an in-plane parameter of 8.42 ± 0.01 Å and an out-of-plane one of 8.412 ± 0.002 Å, both very close to the GeFO bulk cubic parameter of 8.413 ± 0.001 Å. The films show the expected antiferromagnetic behaviour with an ordering temperature of 40 K, which is higher than the ca. 10 K reported in the literature. We suggest that this could be attributed to a different Fe\Ge cationic distribution. We have indeed shown by resonant elastic X-ray diffraction that some of the Fe cations sit in tetrahedral sites and not only in the octahedral sites, as expected from the bulk. The strong A-O-B magnetic exchanges between Fe in the two different sites would indeed explain an increase of the ordering temperature. Finally, we could also provide a way to tune the stoichiometry of the films by changing the laser fluence. We could thus stabilize a highly crystalline $Ge_xFe_{3-x}O_4$ phase with x in the [0.91–1.20] range, and have some control over its ordering transition temperature. We hope that our work will pave the way for exploring the properties of this highly promising frustrated material in thin films, an area that has so far been hindered by the challenge of producing such films.

CRediT authorship contribution statement

L. Schlur: Writing – original draft, Visualization, Validation, Supervision, Software, Resources, Project administration, Methodology, Investigation, Formal analysis, Data curation, Conceptualization. **C. Bouillet:** Writing – original draft, Software, Resources, Methodology, Investigation. **F. Roulland:** Writing – original draft, Resources, Methodology, Investigation. **G. Versini:** Resources, Methodology. **M. Lenertz:** Writing – original draft, Resources, Investigation. **C. Leuvrey:** Resources, Investigation. **J. Robert:** Resources, Investigation. **G.A. Chahine:** Resources. **N. Blanc:** Resources. **A. Peña Corredor:** Writing – original draft, Resources, Investigation. **D. Preziosi:** Writing – original draft, Validation, Investigation, Conceptualization. **C. Lefèvre:** Writing – original draft, Validation, Software, Resources, Investigation. **N. Viart:** Writing – original draft, Visualization, Validation, Supervision, Project administration, Methodology, Investigation, Funding acquisition, Formal analysis, Conceptualization.

Declaration of competing interest

The authors have declared no conflict of interest.

Acknowledgements

The authors wish to thank S. de Brion and L. Chaix (Institut Néel, France) for fruitfull discussions about the material, D. Troadec (IEMN, Lille, France) and A.-M. Blanchenet (UMET, Lille, France) for the preparation of the TEM FIB lamellae, as well as the PLD, XRD, MEB-CRO, TEM and MagTransCS platforms of the IPCMS for providing elaboration and characterization facilities. We also acknowledge the European Synchrotron Radiation Facility for provision of synchrotron radiation facilities and we would like to thank all the staff for assistance in using the beamline BM02-D2AM. Within the Interdisciplinary Thematic Institute QMat, as part of the ITI 2021 2028 program of the University of Strasbourg, CNRS and Inserm, the project was supported by IdEx Unistra (ANR 10 IDEX 0002) and by SFRI STRAT'US project (ANR 20 SFRI 0012) and ANR-11-LABX-0058_NIE and ANR-17-EURE-0024 under the framework of the French Investments for the Future Program. This work was also supported by France 2030 government investment plan managed by the French National Research Agency under grant reference PEPR SPIN – SPINMAT ANR-22-EXSP-0007.

Appendix A. Supplementary data

Supplementary data to this article can be found online at https://doi.org/10.1016/j.matchemphys.2025.130831.

Data availability

Data will be made available on request.

References

[1] C.R. Wiebe, Fantastic frustrated materials–and where to find them, ACS Cent. Sci. 10 (2024) 1811–1812, https://doi.org/10.1021/acscentsci.4c01409.
[2] L. Kubíčková, A.K. Weber, M. Panthöfer, S. Calder, A. Möller, $Cs_2Fe_2(MoO_4)_3$ —A strongly frustrated magnet with orbital degrees of freedom and magnetocaloric properties, Chem. Mater. 36 (2024) 7016–7025, https://doi.org/10.1021/acs.chemmater.4c01262.
[3] Y. Zhao, Z. Ma, Z. He, H. Liao, Y.-C. Wang, J. Wang, Y. Li, Quantum annealing of a frustrated magnet, Nat. Commun. 15 (2024) 3495, https://doi.org/10.1038/s41467-024-47819-y.
[4] H.T. Diep, Theoretical methods for understanding advanced magnetic materials: the case of frustrated thin films, J. Sci. Adv. Mater. Devices 1 (2016) 31–44, https://doi.org/10.1016/j.jsamd.2016.04.009.
[5] T. Lookman, X. Ren (Eds.), Frustrated Materials and Ferroic Glasses, Springer International Publishing, Cham, 2018, https://doi.org/10.1007/978-3-319-96914-5.
[6] H. Takagi, S. Niitaka, Highly frustrated magnetism in spinels, in: C. Lacroix, P. Mendels, F. Mila (Eds.), Introd. Frustrated Magn., Springer Berlin Heidelberg, Berlin, Heidelberg, 2011, pp. 155–175, https://doi.org/10.1007/978-3-642-10589-0_7.
[7] V. Tsurkan, H.-A. Krug Von Nidda, J. Deisenhofer, P. Lunkenheimer, A. Loidl, On the complexity of spinels: magnetic, electronic, and polar ground states, Phys. Rep. 926 (2021) 1–86, https://doi.org/10.1016/j.physrep.2021.04.002.
[8] D.M. Vasiukov, M. Kareev, F. Wen, L. Wu, P. Shafer, E. Arenholz, X. Liu, J. Chakhalian, Epitaxial stabilization of thin films of the frustrated Ge-based spinels, Phys. Rev. Mater. 5 (2021) 064419, https://doi.org/10.1103/PhysRevMaterials.5.064419.
[9] S. Diaz, S. De Brion, G. Chouteau, P. Strobel, B. Canals, J.R. Carvajal, H. Rakoto, J. M. Broto, Magnetic frustration in the spinel compounds GeNi2O4 and GeCo2O4, J. Appl. Phys. 97 (2005) 10A512, https://doi.org/10.1063/1.1863113.
[10] M. Ambrosetti, M. Bini, The renewed interest on brunogeierite, GeFe2O4, a rare mineral of germanium: a review, Molecules 27 (2022) 8484, https://doi.org/10.3390/molecules27238484.
[11] G. Perversi, A.M. Arevalo-Lopez, C. Ritter, J.P. Attfield, Frustration wave order in iron(II) oxide spinels, Commun. Phys. 1 (2018) 69, https://doi.org/10.1038/s42005-018-0067-7.
[12] F. Varret, P. Imbert, Mössbauer study of Fe2+ ions in trigonal sites of spinels: GeFe2O4, GeCo2O4, GeNi2O4, J. Phys. Chem. Solids 35 (1974) 215–222, https://doi.org/10.1016/0022-3697(74)90037-7.
[13] F. Varret, P. Imbert, Mössbauer study of Fe2+ ions in trigonal sites of spinels: GeFe2O4, GeCo2O4, GeNi2O4, J. Phys. Chem. Solids 35 (1974) 215–222, https://doi.org/10.1016/0022-3697(74)90037-7.
[14] G. Blasse, J.F. Fast, Néel temperature of some antiferromagnetic oxides spinel structure, Philips Res. Rep. (1963) 393–399.
[15] P.T. Barton, M.C. Kemei, M.W. Gaultois, S.L. Moffitt, L.E. Darago, R. Seshadri, M. R. Suchomel, B.C. Melot, Structural distortion below the Néel temperature in spinel GeCo 2 O 4, Phys. Rev. B 90 (2014) 064105, https://doi.org/10.1103/PhysRevB.90.064105.
[16] S. Diaz, S. De Brion, G. Chouteau, B. Canals, V. Simonet, P. Strobel, Magnetic frustration in the spinel compounds Ge Co 2 O 4 and Ge Ni 2 O 4, Phys. Rev. B 74 (2006) 092404, https://doi.org/10.1103/PhysRevB.74.092404.
[17] J. Luo, G.-W. Chern, Frustrated Kondo chains and glassy magnetic phases on the pyrochlore lattice, Phys. Rev. B 98 (2018) 214423, https://doi.org/10.1103/PhysRevB.98.214423.
[18] S. Yuvaraj, M.-S. Park, V.G. Kumar, Y.S. Lee, D.-W. Kim, Electrochemical performance of M2GeO4 (M = Co, Fe and Ni) as anode materials with high capacity for lithium-ion batteries, J. Electrochem. Sci. Technol. 8 (2017) 323–330, https://doi.org/10.33961/JECST.2017.8.4.323.
[19] Y. Subramanian, M.-S. Park, G.K. Veerasubramani, Y.-S. Lee, D.-W. Kim, Synthesis and electrochemical performance of carbon-coated Fe2GeO4 as an anode material for sodium-ion batteries, Mater. Chem. Phys. 224 (2019) 129–136, https://doi.org/10.1016/j.matchemphys.2018.12.007.
[20] J. Han, J. Qin, L. Guo, K. Qin, N. Zhao, C. Shi, E. Liu, F. He, L. Ma, C. He, Ultrasmall Fe_2GeO_4 nanodots anchored on interconnected carbon nanosheets as high-performance anode materials for lithium and sodium ion batteries, Appl. Surf. Sci. 427 (2018) 670–679, https://doi.org/10.1016/j.apsusc.2017.08.026.
[21] H. Choi, S. Surendran, D. Kim, Y. Lim, J. Lim, J. Park, J.K. Kim, M.-K. Han, U. Sim, Boosting eco-friendly hydrogen generation by urea-assisted water electrolysis using spinel M2GeO4 (M = Fe, Co) as an active electrocatalyst, Environ. Sci. Nano 8 (2021), https://doi.org/10.1039/d1en00529d.
[22] P. Strobel, F.P. Koffyberg, A. Wold, Electrical and optical properties of high-purity p-type single crystals of GeFe2O4, J. Solid State Chem. 31 (1980) 209–216, https://doi.org/10.1016/0022-4596(80)90022-5.
[23] T. Setkova, A. Spivak, E.Y. Borovikova, M.V. Voronin, E.S. Zakharchenko, V. S. Balitsky, A. Kuzmin, L. Sipavina, A. Iskrina, S.S. Khasanov, Synthetic brunogeierite Fe2GeO4: XRD, Mossbauer and Raman high-pressure study,

Spectrochim. Acta Part -Mol. Biomol. Spectrosc. 267 (2022) 120597, https://doi.org/10.1016/j.saa.2021.120597.
[24] P.A. Sossi, B. Fegley Jr., Thermodynamics of element volatility and its application to planetary processes, Rev. Mineral. Geochem. 84 (2018) 393–459, https://doi.org/10.2138/rmg.2018.84.11.
[25] M. Seki, M. Takahashi, T. Ohshima, H. Yamahara, H. Tabata, High spin polarization at room temperature in Ge-substituted Fe3O4 epitaxial thin film grown under high oxygen pressure, Appl. Phys. Lett. 103 (2013) 212404, https://doi.org/10.1063/1.4832062.
[26] S. Abe, Improved resistance to oxidation of Ge-doped Fe3O4 thin films with cation excess composition using a sputtering target of FeO, AIP Adv. 12 (2022) 095213, https://doi.org/10.1063/5.0102338.
[27] K. Shinoda, S. Abe, K. Sugiyama, Y. Waseda, The local structure around Ge atoms in Ge-doped magnetite thin films, High Temp. Mater. Process. 39 (2020) 645–662, https://doi.org/10.1515/htmp-2020-0099.
[28] M. Seki, H. Tabata, H. Ohta, K. Inaba, S. Kobayashi, Epitaxial thin films of p-type spinel ferrite grown by pulsed laser deposition, Appl. Phys. Lett. 99 (2011), https://doi.org/10.1063/1.3670045.
[29] G.A. Chahine, N. Blanc, S. Arnaud, F. De Geuser, R. Guinebretière, N. Boudet, Advanced non-destructive in situ characterization of metals with the French collaborating research group d2am/BM02 beamline at the European synchrotron radiation facility, Metals 9 (2019) 352, https://doi.org/10.3390/met9030352.
[30] C. Lefevre, A. Thomasson, F. Roulland, V. Favre-Nicolin, Y. Joly, Y. Wakabayashi, G. Versini, S. Barre, C. Leuvrey, A. Demchenko, N. Boudet, N. Viart, Determination of the cationic distribution in oxidic thin films by resonant X-ray diffraction: the magnetoelectric compound $Ga_{2-x}Fe_xO_3$, J. Appl. Crystallogr. 49 (2016) 1308–1314, https://doi.org/10.1107/S1600576716010001.
[31] D. Dijkkamp, T. Venkatesan, X.D. Wu, S.A. Shaheen, N. Jisrawi, Y.H. Min-Lee, W. L. McLean, M. Croft, Preparation of Y-Ba-Cu oxide superconductor thin films using pulsed laser evaporation from high Tc bulk material, Appl. Phys. Lett. 51 (1987) 619–621, https://doi.org/10.1063/1.98366.
[32] H.-U. Krebs, M. Weisheit, J. Faupel, E. Süske, T. Scharf, C. Fuhse, M. Störmer, K. Sturm, M. Seibt, H. Kijewski, D. Nelke, E. Panchenko, M. Buback, Pulsed laser deposition (PLD) – A versatile thin film technique, in: B. Kramer (Ed.), Adv. Solid State Phys., Springer, Berlin, Heidelberg, 2003, pp. 505–518, https://doi.org/10.1007/978-3-540-44838-9_36.
[33] T. Ohnishi, K. Shibuya, T. Yamamoto, M. Lippmaa, Defects and transport in complex oxide thin films, J. Appl. Phys. 103 (2008) 103703, https://doi.org/10.1063/1.2921972.
[34] L.-G. Liu, High-pressure phases of Co2GeO4, Ni2GeO4, Mn2GeO4 and MnGeO3: implications for the germanate-silicate modeling scheme and the Earth's mantle, Earth Planet Sci. Lett. 31 (1976) 393–396, https://doi.org/10.1016/0012-821X(76)90120-5.
[35] G. Perversi, A.M. Arevalo-Lopez, C. Ritter, J.P. Attfield, Frustration wave order in iron(II) oxide spinels, Commun. Phys. 1 (2018) 69, https://doi.org/10.1038/s42005-018-0067-7.
[36] R. Valenzuela, Magnetic Ceramics, Cambridge University Press, Cambridge, 1994, https://doi.org/10.1017/CBO9780511600296.
[37] D.J. Wales, J.P.K. Doye, Global optimization by Basin-Hopping and the lowest energy structures of Lennard-Jones clusters containing up to 110 atoms, J. Phys. Chem. A 101 (1997) 5111–5116, https://doi.org/10.1021/jp970984n.
[38] O. Bunău, Y. Joly, Self-consistent aspects of x-ray absorption calculations, J. Phys. Condens. Matter 21 (2009) 345501, https://doi.org/10.1088/0953-8984/21/34/345501.
[39] D. Preziosi, A. Sander, A. Barthélémy, M. Bibes, Reproducibility and off-stoichiometry issues in nickelate thin films grown by pulsed laser deposition, AIP Adv. 7 (2017) 015210, https://doi.org/10.1063/1.4975307.